Optics
2026, Vol. 14, No. 1, pp. 22–31
https://doi.org/10.11648/j.optics.20261401.12

Letter

Compact Two-dimensional-ultrawide-field-of-view Broadband High-spectral-resolution Snapshot Imaging Spectrometer

Qinghua Yang[1, *], Zhipeng Wang[2]

[1]School of Optoelectronic Engineering, Xidian University, Xi'an, China
[2]Command and Communication Department, Northern Lianchuang Communication Company Limited, Nanchang, China

Abstract

For wide-area reconnaissance and surveillance systems, ultrawide field of view, real-time measurement and compact size are very important. This article presents a compact two-dimensional-ultrawide-field-of-view broadband high-spectral-resolution snapshot imaging spectrometer (*2DUFBHSIS*), which consists of an imaging microlens array, multiple optical fibers, seven identical collimating microlens arrays, seven identical optical filters, seven identical planar transmission gratings, and seven identical detectors. The imaging microlens array is divided into seven identical parts in the horizontal direction, each part coupled to a separate collimating microlens array through optical fibers. The 2DUFBHSIS employs a parallel architecture to effectively balance key performance requirements, including ultrawide field of view, broad spectral coverage, high spectral resolution, real-time spectral imaging and a compact overall design. The theoretical analysis and simulation results are provided to demonstrate the feasibility of the proposed concept. The 2DUFBHSIS can simultaneously achieve two-dimensional ultrawide-field-of-view (e.g. 105°×80°), broad spectral range (e.g. 350 nm), high spectral resolution (superior to 10 nm in the wavelength range of 400 nm to 750 nm), real-time measurement, and compact size (e.g. overall size is less than 130 mm × 100 mm × 100 mm). The 2DUFBHSIS has great potential for wide-area optical reconnaissance and surveillance on remote sensing platforms (e.g., unmanned aerial vehicles and helicopters).

Keywords

Snapshot Imaging Spectrometer, Two-dimensional Ultrawide-field-of-view, Compact Size, Broad Spectral Range, High Spectral Resolution

1. Introduction

For wide-area reconnaissance and surveillance systems, especially for remote sensing optoelectronic reconnaissance sensors, the following three points are extremely important. Firstly, in order to meet the requirements of wide-area search, a two-dimensional (2D) ultrawide field of view (FOV) is very important. Secondly, in order to meet the requirements of rapid detection, particularly for detecting the dynamic targets with rapidly changing spectral features or spatial positions

*Correspondence: Qinghua Yang (yangqh812@126.com)

Received: 26 June 2026; **Accepted:** 8 July 2026; **Published:** 24 July 2026

Copyright: © The Author(s), 2026. Published by Science Publishing Group. This is an **Open Access** article, distributed under the terms of the Creative Commons Attribution 4.0 License (http://creativecommons.org/licenses/by/4.0/), which permits unrestricted use, distribution and reproduction in any medium, provided the original work is properly cited.

such as explosions, rapid combustion or missile plumes, real-time measurement is equally crucial. Thirdly, for airborne or satellite-borne optoelectronic sensors, high stability and compact size are also very important.

Traditional optical imagers generally achieve an ultrawide FOV by using the methods such as fisheye lens [1, 2], catadioptric panoramic lens [3-8], monocentric multiscale cameras [9-15], artificial compound eyes [16-21], or panoramic monocentric fiber-coupled imagers [22-26]. However, these methods cannot obtain high-resolution spectral information.

Existing 2D-ultrawide-FOV broadband high-spectral-resolution imaging spectrometers are all scanning types: either they use a front-mounted scanning mirror [27, 28] to achieve a 2D ultrawide FOV and acquire broadband high-resolution spectral information in real time, or they use a front-mounted scanning mirror to achieve a 2D ultrawide FOV and acquire broadband high-resolution spectral information in either a time-scanning mode or wavelength-s canning mode, or they acquire broadband high-resolution spectral information in a scanning manner and obtain a 2D ultrawide FOV in real time [29]. Their common drawback is that the measurement time is long, which requires at least one scanning cycle, making real-time measurement impossible.

For a 2D-ultrawide-FOV broadband high-spectral-resolution imaging spectrometer based on a scanning Michelson-type interferometer [29], besides being unable to achieve real-time measurement, the presence of moving parts and drive systems leads to low stability and a bulky design (uncompact structure).

For an ultrawide-FOV high-resolution snapshot imaging spectrometer that utilizes a one-dimensional microlens array to obtain a one-dimensional ultrawide FOV and uses a static grating interferometer (SGI) to acquire high-resolution spectral information [30], since the number of sampling points of each interferogram obtained by the SGI is relatively small, its spectral range is too narrow to achieve a broad wavelength range exceeding 200 nm.

Other snapshot imaging spectrometers can either achieve compact size [31, 32], or broad spectral range [33, 34], or high spectral resolution [35], or high spatial resolution [36, 37], but none of them can achieve both a 2D ultrawide FOV and broadband real-time spectral imaging.

2. Principle

This letter presents a compact two-dimensional-ultrawide-field-of-view broadband high-spectral-resolution snapshot imaging spectrometer (*2DUFBHSIS*). Figure 1 shows the optical layout of the 2DUFBHSIS. It contains an imaging microlens array (*MLA1*), multiple optical fibers, seven identical collimating microlens arrays (*MLA2*～*MLA8*) arranged sequentially along the *y*-axis direction, seven identical optical filters (*F1*～*F7*) arranged sequentially along the *y*-axis direction, seven identical planar transmission gratings (*G1*～*G7*) arranged one after another along the *y*-axis direction, and seven identical detectors (*D1*～*D7*) arranged one after another along the *y*-axis in the *x*-*y* plane.

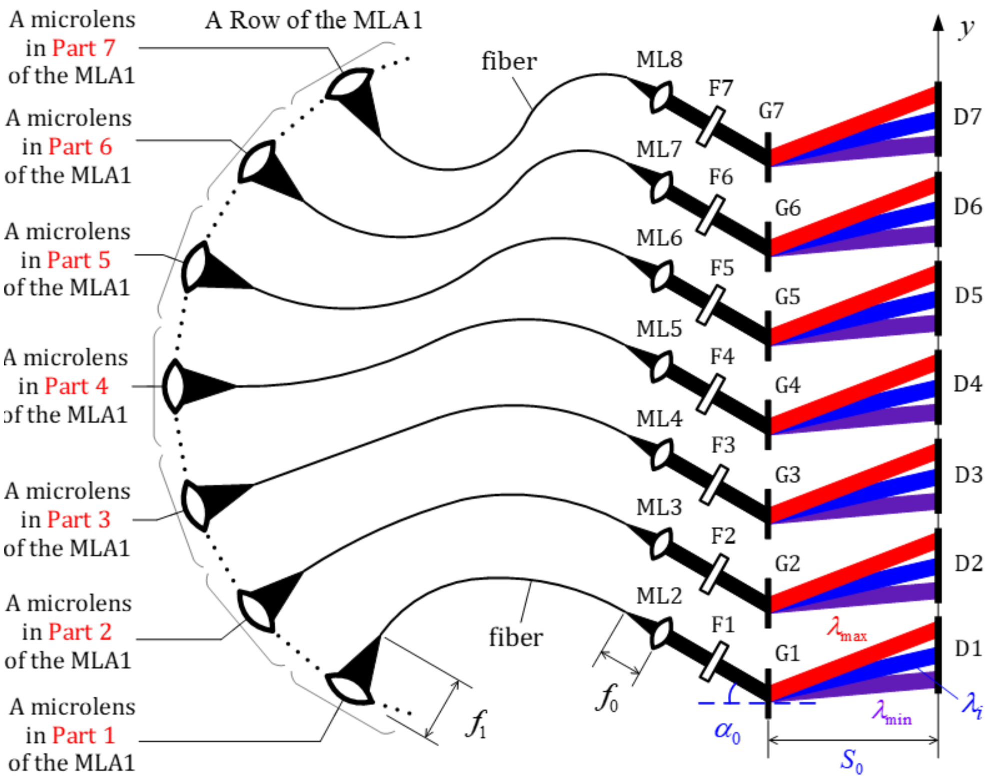

Figure 1. *Optical layout of the compact 2DUFBHSIS.*

MLA1 includes q_1 columns and q_2 rows of microlenses. Each row of MLA1 is arranged on circular arcs in different planes to obtain an ultrawide FOV in the horizontal plane in real time. Each column of MLA1 is arranged on circular arcs in different vertical planes to obtain an ultrawide FOV in the vertical plane in real time. Thus, the 2DUFBHSIS can obtain a 2D ultrawide FOV (e.g. 105°×80°) in real time.

MLA1 is divided into seven identical parts (*Part 1*～*Part 7*) in the horizontal direction, each part containing $q_1/7$ columns and q_2 rows of microlenses. The Part *k* of the MLA1 is coupled to microlens array MLA(*k*+1), and each microlens of the Part *k* of the MLA1 is coupled to a separate microlens ML(*k*+1) of microlens array MLA(*k*+1) through a separate fiber, where *k* =1, 2, …, 7.

The light collected by each microlens of the Part *k* of the MLA1 passes sequentially through a separate fiber, a separate microlens ML(*k*+1) of the MLA(*k*+1), filter F*k*, grating G*k*, and finally is received by detector D*k*, where *k* =1, 2, …, 7.

Suppose that Φ_1 is the horizontal FOV of the 2DUFBHSIS, Φ_2 is the vertical FOV of the 2DUFBHSIS, ϕ is the FOV of each microlens of MLA1, f_1 is the focal length of each microlens of MLA1, and r is the radius of the circular arcs formed by each column (row) of MLA1.

The aperture size D_1 of each microlens of MLA1 should be

$$D_1 < \pi\phi r/180° \tag{1}$$

The number of microlenses in each row of MLA1 is $q_1 = \Phi_1/\phi$. The number of microlenses in each column of MLA1 is $q_2 = \Phi_2/\phi$. The Part *k* of the MLA1 has a horizontal FOV of $\Phi_1/7$, a vertical FOV of Φ_2, and contains $\Phi_1/7\phi$ columns and Φ_2/ϕ rows of microlenses.

MLA(*k*+1) includes multiple microlenses arranged in a straight line parallel to the *x*-axis direction, where *k* =1, 2, …, 7. Figure 2 shows the schematic diagram of the positional relationship between a column of the Part *k* of the MLA1 and microlens array MLA(*k*+1). Figure 3 shows the schematic diagram of the positional relationship between the Part *k* of the MLA1 and microlens array MLA(*k*+1). W_0 is the size in the x-axis direction of multiple microlenses ML(*k*+1) that are coupled with a column of the Part *k* of the MLA1.

The q_2 microlenses located in the *n*-th column of the Part *k* of the MLA1 are respectively coupled to the microlenses ML(*k*+1) numbered $(n-1)q_2+1,\ (n-1)q_2+2,\ \cdots,\ nq_2$, where $n = 1,\ 2,\ \cdots,\ q_1/7$.

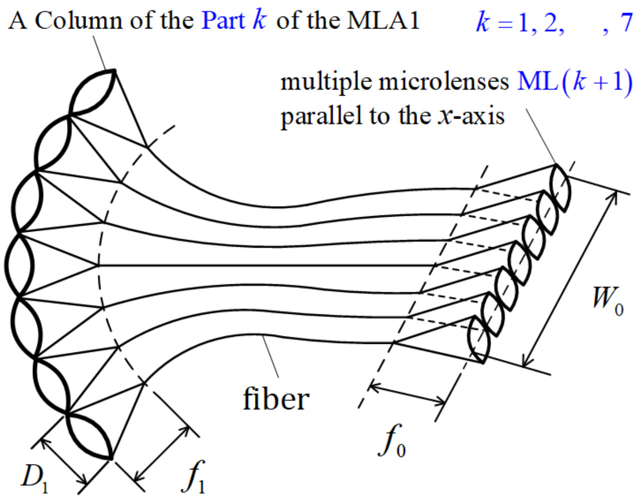

Figure 2. *Schematic diagram of the positional relationship between a column of the Part k of the MLA1 and microlens array MLA(k+1).*

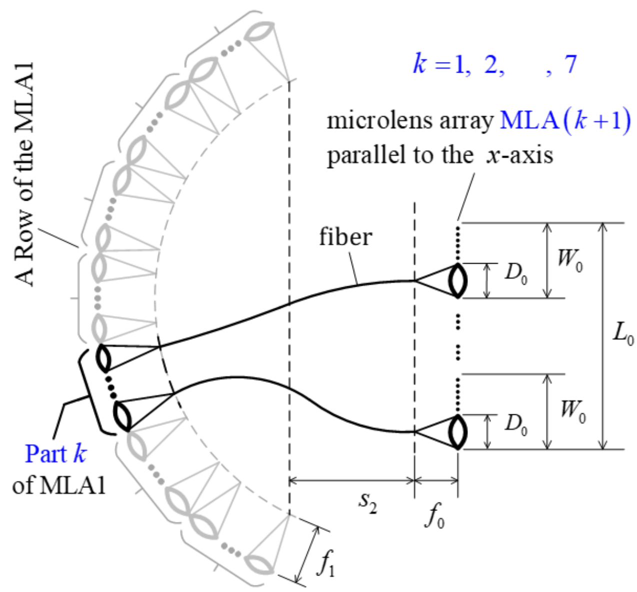

Figure 3. *Schematic diagram of the positional relationship between the Part k of the MLA1 and microlens array MLA(k+1).*

The optical axis of each microlens of MLA(*k*+1) is perpendicular to the grating grooves of grating G*k*. The angle between the optical axis of each microlens of MLA(*k*+1) and the normal of grating G*k* is α_0. The aperture size of each microlens of MLA(*k*+1) is D_0. The focal length of each microlens of MLA(*k*+1) is f_0. The center distance between two adjacent microlenses of MLA(*k*+1) is τ_0, where $\tau_0 > D_0$ and τ_0 should be an integer multiple of the detector pixel size.

The number of microlenses of MLA(*k*+1) is given by

$$Q_0 = q_1 q_2 / 7 = \Phi_1 \Phi_2 / \left(7\phi^2\right) \quad (2)$$

The size in the *x*-axis direction of MLA(*k*+1) is given by

$$L_0 = Q_0 \tau_0 = \Phi_1 \Phi_2 \tau_0 / \left(7\phi^2\right) \quad (3)$$

The angular resolution of the 2DUFBHSIS is

$$\delta\phi = \phi \quad (4)$$

Filter F1 to F7 allow only the light in the wavelength range $(\lambda_{\min}, \lambda_{\max})$ to pass through, where $\lambda_{\min}$ and $\lambda_{\max}$ are the minimum and maximum wavelengths that can be resolved by the 2DUFBHSIS, respectively. The 2DUFBHSIS uses the first-order diffraction of the grating, so the spectral range of the 2DUFBHSIS must satisfy

$$\lambda_{\max} < 2\lambda_{\min} \quad (5)$$

Grating G1 to G7 are located in the same plane parallel to the *x-y* plane. The grating grooves of grating G1 to G7 are parallel to the *x*-axis. Detector D1 to D7 are located in the *x-y* plane. Each column of detector D*k* is parallel to the *y*-axis. The grating G*k* is parallel to detector D*k*.

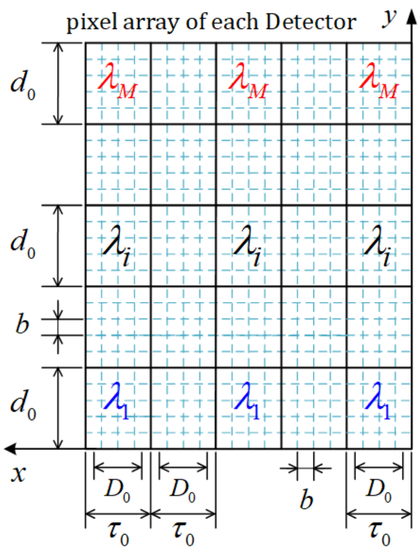

Figure 4*. Schematic diagram of both spatial image distribution and spectral distribution on each detector pixel array.*

Figure 4 shows the schematic diagram of spatial image distribution and spectral distribution on each detector pixel array. λ_1 is the first wavelength (the minimum wavelength $\lambda_{\min}$) resolved by the 2DUFBHSIS, λ_i is the i-th wavelength resolved by the 2DUFBHSIS, λ_M is the M-th wavelength (the maximum wavelength $\lambda_{\max}$) resolved by the 2DUFBHSIS. M is the number of wavelengths that can be resolved by the 2DUFBHSIS. b is the pixel size of each detector. d_0 is the length in the *y*-axis direction of the illuminated region on detector D*k* for each wavelength resolved by the 2DUFBHSIS, and $d_0 = D_0 / \cos\alpha_0$.

Each detector is divided into multiple blocks arranged in M rows and Q_0 columns, each block has a size of $d_0 \times \tau_0$, and each block contains $d_0 / b \times \tau_0 / b$ pixels. Each column of blocks in detector D*k* records spatial and spectral information of a separate object unit collected by a separate microlens of the Part *k* of the MLA1.

The aperture size of each microlens of MLA(*k*+1) is

$$D_0 = d_0 \cos\alpha_0 \quad (6)$$

The size in the *x*-axis direction of filter F*k* should satisfy

$$L_{Fx} > \Phi_1 \Phi_2 \tau_0 / \left(7\phi^2\right) \quad (7)$$

The size in the *x*-axis direction of grating G*k* should be

$$L_{Gx} > \Phi_1 \Phi_2 \tau_0 / \left(7\phi^2\right) \quad (8)$$

The size in the *y*-axis direction of grating G*k* should be

$$L_{Gy} > d_0 \quad (9)$$

The size in the *x*-axis direction of detector D*k* is

$$L_{Dx} = \Phi_1 \Phi_2 \tau_0 / \left(7\phi^2\right) \quad (10)$$

The size in the *y*-axis direction of detector D*k* is

$$L_{Dy} = M d_0 \quad (11)$$

The overall size in the *x*-axis direction of the 2DUFBHSIS should satisfy

$$L_x > \Phi_1 \Phi_2 \tau_0 / \left(7\phi^2\right) \quad (12)$$

The overall size in the *y*-axis direction of the 2DUFBHSIS can be estimated by

$$L_y > 7 \times \max\left\{ s_1 \tan\alpha_0 + D_0/2,\ M d_0 + h_0 \right\} \quad (13)$$

where s_1 is the distance from the center of a microlens of MLA(*k*+1) to grating G*k* in the *z*-axis direction (perpendicular to the *x*-*y* plane), and h_0 is the distance in the *y*-axis direction between the lowest point on detector Dk of the first-order diffracted light of the minimum wavelength $\lambda_{\min}$ and the grating normal located at the lowest point of grating Gk surface illuminated by the incident parallel beam.

The overall size in the *z*-axis direction (perpendicular to the *x*-*y* plane) of the 2DUFBHSIS can be estimated by

$$L_z > S_0 + s_1 + f_0 \cos\alpha_0 + s_2 + \left[r - (r - f_1)\cos(\Phi_1/2)\right] \quad (14)$$

where, as shown in Figure 3, s_2 is the distance between the straight line passing through the focal points of the two microlenses located at both ends of a row of the MLA1 and the plane formed by the focal points of all collimating microlenses.

The distance S_0 between grating Gk and detector Dk is

$$S_0 = \frac{d_0}{\tan\left[\arcsin\left(\lambda_{\min}/g + \Delta\lambda_0/g - \sin\alpha_0\right)\right] - p_0} \quad (15)$$

$$p_0 = \tan\left[\arcsin\left(\lambda_{\min}/g - \sin\alpha_0\right)\right] \quad (16)$$

where g is the groove spacing (grating period) of grating Gk, and $\Delta\lambda_0$ is the spectral resolution of the 2DUFBHSIS at the minimum wavelength $\lambda_{\min}$. In addition, h_0 is given by

$$h_0 = \frac{d_0 \cdot p_0}{\tan\left[\arcsin\left(\lambda_{\min}/g + \Delta\lambda_0/g - \sin\alpha_0\right)\right] - p_0} \quad (17)$$

The spectral resolution of the 2DUFBHSIS at the i-th wavelength λ_i can be expressed as

$$\begin{aligned}\Delta\lambda_i &= g\sin\left\{\arctan\left(\frac{id_0}{S_0} + p_0\right)\right\} \\ &\quad - g\sin\left\{\arctan\left[\frac{(i-1)d_0}{S_0} + p_0\right]\right\}\end{aligned} \quad (18)$$

where $i = 1,\ 2,\ \cdots,\ M$.

According to the definition of the resolving power of a grating and the formula of the theoretical maximum resolving power of a planar grating, the spectral resolution of the 2DUFBHSIS at the wavelength λ_i should also satisfy

$$\Delta\lambda_i \geq g\lambda_i / d_0 \quad (19)$$

The intensity of the first-order diffracted light of the 2DUFBHSIS at wavelength λ is approximately given by

$$I(\lambda) = \int_{y_1}^{y_2} \frac{a^2 P(\lambda)\cos^2\alpha}{d_0 \lambda S_0^2} \left(\frac{\sin \pi d_0/g}{\sin\pi}\right)^2 \left(\frac{g}{\pi a}\sin\frac{\pi a}{g}\right)^2 dy \quad (20)$$

$$y_1 = S_0\left[\tan\alpha_0 + \tan\left(\arcsin\left(\lambda/g - \sin\alpha_0\right)\right)\right] \quad (21)$$

$$y_2 = d_0 + S_0\left[\tan\alpha_0 + \tan\left(\arcsin\left(\lambda/g - \sin\alpha_0\right)\right)\right] \quad (22)$$

where a is the transmission width per grating period of transmission grating, and $P(\lambda)$ is the total intensity incident on grating Gk at wavelength λ for the output beam of a microlens of MLA(*k*+1).

Suppose that $\Delta\alpha$ is the alignment error angle of the collimating microlens array along the *y*-axis direction, the angle between the optical axis of each microlens of MLA(*k*+1) and the normal of grating G*k* is $\alpha' = \alpha_0 + \Delta\alpha$, and the angle of incidence to the grating G*k* is $\alpha' = \alpha_0 + \Delta\alpha$. The spectral resolution of the 2DUFBHSIS at the i-th wavelength λ_i, including the alignment error of the collimating microlens array in the *y*-axis direction, can be approximately calculated by

$$\begin{aligned}\Delta\lambda_i' &= g\sin\left[\arctan\left(\frac{id_0\cos\alpha_0}{S_0\cos\alpha'} + p_0\right)\right] \\ &\quad - g\sin\left\{\arctan\left[\frac{(i-1)d_0\cos\alpha_0}{S_0\cos\alpha'} + p_0\right]\right\}\end{aligned} \quad (23)$$

The error of spectral resolution of the 2DUFBHSIS at wavelength λ_i, generated by the alignment error of the collimating microlens array in the *y*-axis direction, can be given by

$$E\lambda_i = \Delta\lambda_i' - \Delta\lambda_i \quad (24)$$

Small alignment errors of the collimating microlens array in the *x*-axis direction have almost no effect on the spectral resolution of the 2DUFBHSIS.

In practical applications, the value of τ_0 should satisfy $\tau_0 = \lceil D_0/b \rceil + 2b \cdot N$, where N is a positive integer, and so the minimum value of τ_0 is $\tau_0 = \lceil D_0/b \rceil + 2b$. In order to better eliminate the impact of the channel crosstalk and the alignment error in the *x*-axis direction, it can also be set as $\tau_0 = \lceil D_0/b \rceil + 4b$ or $\tau_0 = \lceil D_0/b \rceil + 6b$.

When the optical throughput needs to be increased, the aperture size D_1 of each microlens of MLA1 needs to be increased, a 2D ultrawide FOV will lead to an increase in size of MLA1. To increase the optical throughput, the 2DUFBHSIS can slightly reduce the field of view to control the instrument size, making it better for wide-area optical reconnaissance and surveillance on remote sensing platforms.

3. Simulation

Suppose that the spectral range is 400 nm to 750 nm, the spectral resolution at wavelength 400 nm is $\Delta\lambda_0 = 10$ nm, the horizontal FOV is $\Phi_1 = 105°$, the vertical FOV is $\Phi_2 = 80°$, the FOV of each microlens of MLA1 is $\phi = 1°$, and the pixel size of each detector is $b = 0.01$ mm. The angular resolution is $\delta\phi = 1°$, the number of microlenses in each row of MLA1 is $q_1 = 105°/1° = 105$, the number of microlenses in each column of MLA1 is $q_2 = 80°/1° = 80$. Each part of MLA1 has a horizontal FOV of 15°, a vertical FOV of 80°, and contains 15 columns × 80 rows of microlenses. The radius of the circular arcs formed by each column (row) of MLA1 is $r = 80$ mm. The aperture size of each microlens of MLA1 is $D_1 = 0.7$ mm. The focal length of each microlens of MLA1 can be $f_1 = 30$ mm.

The groove spacing of grating Gk is $g = 0.5$ μm. The length in the y-axis direction of the illuminated region on detector Dk for each wavelength resolved by the 2DUFBHSIS is $d_0 = 0.13$ mm. The angle between the optical axis of each microlens in MLA(k+1) and the grating normal of grating Gk is $\alpha_0 = 53.1°$. The distance between grating Gk and detector Dk is $S_0 = 6.5$ mm. In addition, $h_0 = 0.002$ mm.

The number of microlenses of MLA(k+1) is $Q_0 = 1200$. The aperture size of each microlens of MLA(k+1) is $D_0 = 0.078$ mm. The focal length of each microlens of MLA(k+1) can be $f_0 = 1$ mm. The center distance between two adjacent microlenses of MLA(k+1) can be $\tau_0 = 0.1$ mm.

The size in the x-axis direction of filter Fk should satisfy $L_{Fx} > 120$ mm, so it can be $L_{Fx} = 125$ mm. The size of grating Gk can be $L_{Gx} = 125$ mm and $L_{Gy} = 3$ mm.

Figure 5 shows the spectral resolution of the 2DUFBHSIS. The number of wavelengths that can be resolved by the 2DUFBHSIS in the wavelength range from 400 nm to 750 nm is $M = 50$. The spectral resolution of the 2DUFBHSIS in the wavelength range from 400 nm to 750 nm is approximately 10 nm ~ 3.6 nm.

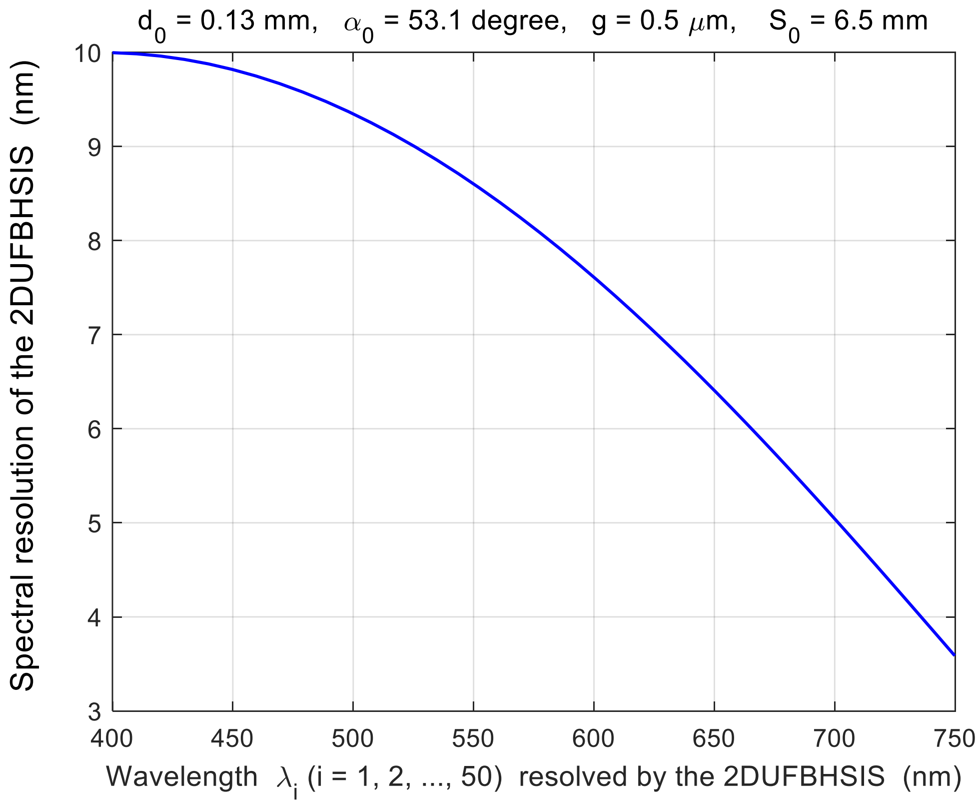

Figure 5. *Spectral resolution of the 2DUFBHSIS.*

Figure 6 shows a comparison between the calculated spectral information and input spectral information in the wavelength range of 400 nm to 750 nm, where the 50 wavelengths resolved by the 2DUFBHSIS are used as the sampling points and randomly assigned normalized spectral intensity to create an input spectral profile, and the calculated spectral information is obtained from a simulation on the above input spectral information and contains only the above 50 wavelengths.

Figure 7 shows a comparison between the calculated spectral information and input spectral information in the wavelength range of 400 nm to 750 nm, where the input spectral information comprises about 50×100 wavelengths selected from the input spectral profile shown in Figure 6, but the calculated spectral information contains only the 50 wavelengths resolved by the 2DUFBHSIS.

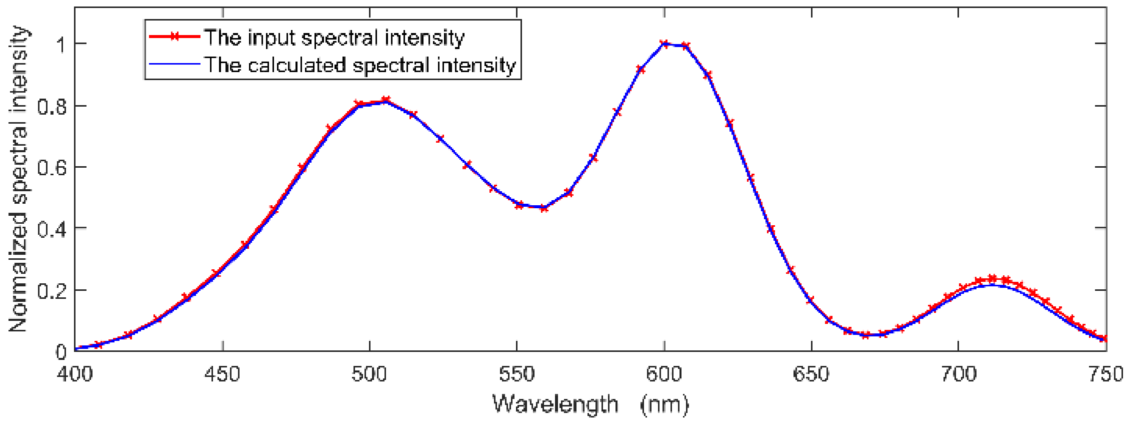

Figure 6. *Comparison between the calculated spectral information and input spectral information in the wavelength range of 400 nm to 750 nm, where the input spectral information comprises only 50 wavelengths resolved by the 2DUFBHSIS, and the calculated spectral information contains only the above 50 wavelengths.*

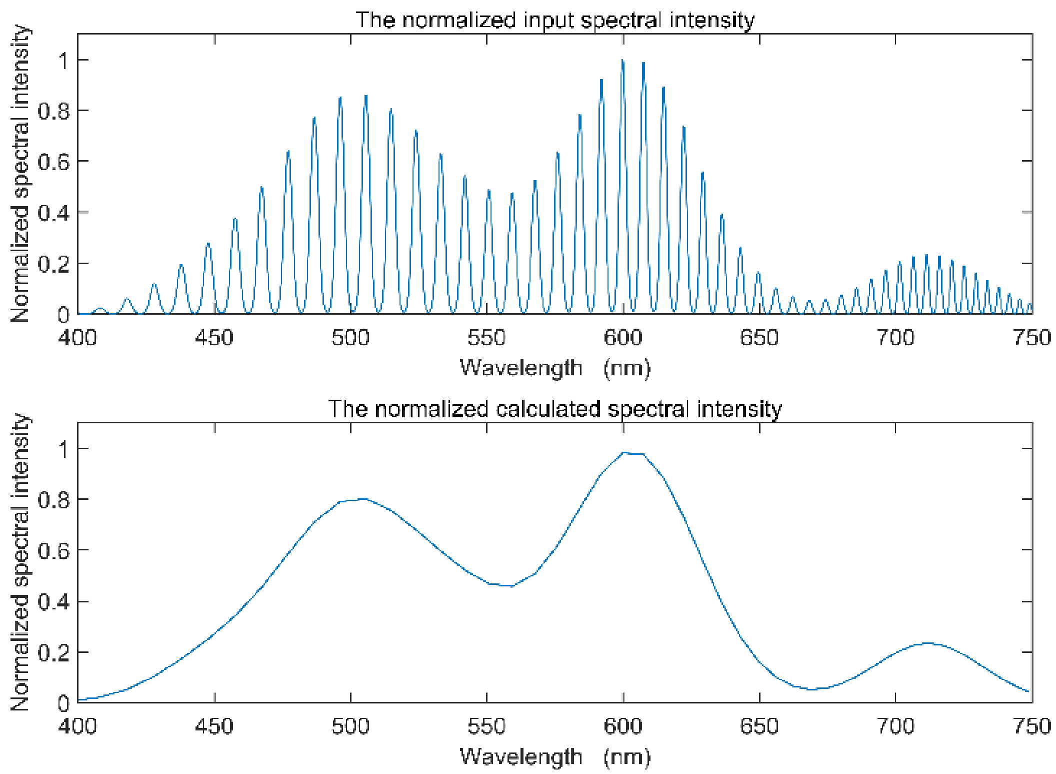

Figure 7. *Comparison between the calculated spectral information and input spectral information in the wavelength range of 400 nm to 750 nm, where the input spectral information contains about 50×100 wavelengths selected from the input spectral profile shown in Figure 6, but the calculated spectral information contains only the 50 wavelengths resolved by the 2DUFBHSIS.*

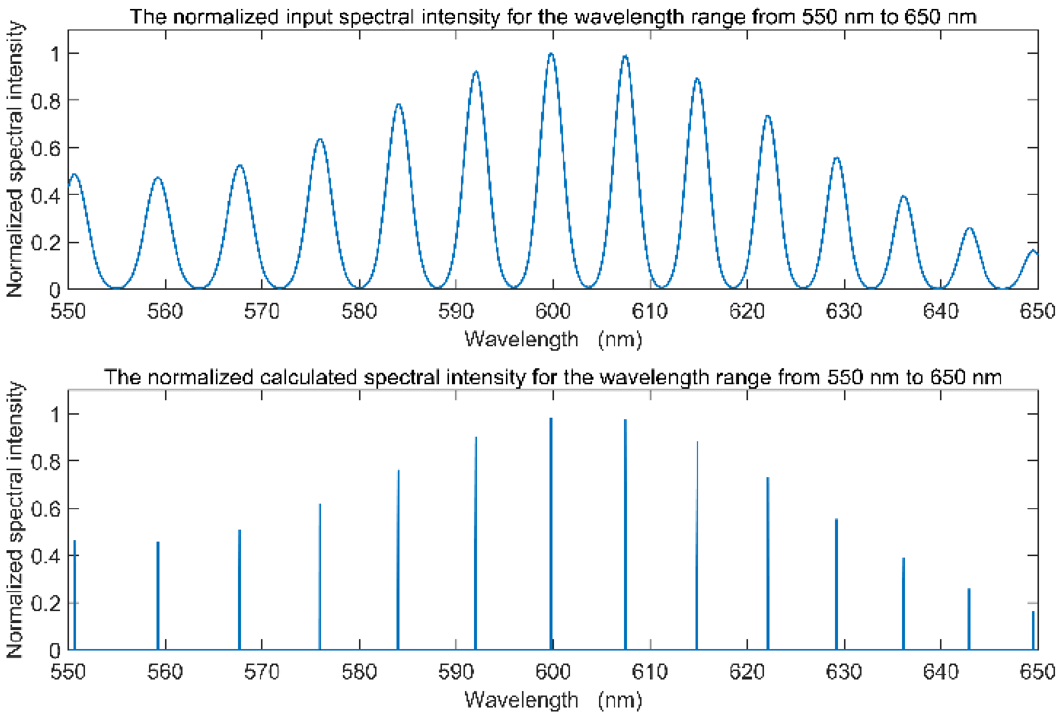

Figure 8. *Comparison between the calculated spectral information and input spectral information in the wavelength range of 550 nm to 650 nm, where the input spectral information comprises about 14×100 wavelengths selected from the input spectral profile shown in Figure 6, but the calculated spectral information contains only the 14 wavelengths resolved by the 2DUFBHSIS.*

Figure 8 shows a comparison between the calculated spectral information and input spectral information in the wavelength range of 550 nm to 650 nm, where the input spectral information comprises about 14×100 wavelengths selected from the input spectral profile shown in Figure 6 in the wavelength range of 550 nm to 650 nm, but the calculated spectral information contains only 14 wavelengths resolved by the 2DUFBHSIS in the wavelength range of 550 nm to 650 nm.

According to Eqs. (12)-(14), the overall size of the 2DUFBHSIS can be less than 130 mm in the *x*-axis direction, less than 100 mm in the *y*-axis direction, and less than 100 mm in the *z*-axis direction perpendicular to the *x*-*y* plane.

Since the value of s_1 can be small and $S_0 = 6.5$ mm, setting $\tau_0 = \lceil D_0/b \rceil + 2b$ is sufficient to eliminate the impact of the channel crosstalk and the alignment error in the *x*-axis direction.

4. Conclusions

The principle of the 2DUFBHSIS was described, the first-order approximations of system performance were given, and a simulation of an example was shown.

Compared with the existing 2D-ultrawide-FOV broadband high-spectral-resolution imaging spectrometers that are all scanning types, the 2DUFBHSIS can achieve real-time measurement and is compact and stable. Compared with the one-dimensional ultrawide-FOV high-resolution snapshot imaging spectrometer [30], the 2DUFBHSIS can achieve both a much wider spectral range (e.g. 350 nm) and a 2D ultrawide FOV (e.g. 105 °×80 °) in real time.

The 2DUFBHSIS can simultaneously achieve 2D ultrawide FOV (e.g. 105 °×80 °), broad spectral range (e.g. 350 nm and above), high spectral resolution (superior to 10 nm in the wavelength range of 400 nm to 750 nm), real-time measurement, and compact size (e.g. overall size can be less than 130 mm × 100 mm × 100 mm). The 2DUFBHSIS has significant potential for wide-area optical reconnaissance and surveillance on remote sensing platforms (e.g., unmanned aerial vehicles, helicopters, and satellites).

Abbreviations

2DUFBHSIS	Two-dimensional-ultrawide-field-of-view Broadband High-spectral-resolution Snapshot Imaging Spectrometer
FOV	Field of View
2D	Two-dimensional
SGI	Static Grating Interferometer

MLA1	Imaging Microlens Array
MLA2~MLA8	Seven Identical Collimating Microlens Arrays
MLA(*k*+1)	Collimating Microlens Array (*k*+1), Where *k* =1, 2, …, 7
ML(*k*+1)	A Microlens of the Collimating Microlens Array (*k*+1), where *k* =1, 2, …, 7
F1~F7	Seven Identical Optical Filters
F*k*	Optical Filter *k*, Where *k* =1, 2, …, 7
G1~G7	Seven Identical Planar Transmission Gratings
G*k*	Planar Transmission Grating *k*, where *k* =1, 2, …, 7
D1~D7	Seven Identical Detectors
D*k*	Detector *k*, where *k* =1, 2, …, 7

Author Contributions

Qinghua Yang: Conceptualization, Funding acquisition, Investigation, Methodology, Writing – original draft, Writing – review & editing

Zhipeng Wang: Data curation, Software

Funding

This work is supported by the Fundamental Research Funds for the Central Universities (Grant No. QTZX25020) and National Natural Science Foundation of China (NSFC) (Grant No. 61605151).

Data Availability Statement

The data is available from the corresponding author upon reasonable request.

Conflicts of Interest

The authors declare no conflicts of interest.

References

[1] K. Miyamoto. Fish Eye Lens. J. Opt. Soc. Am. 1964, 54(8), 1060-1061. https://doi.org/10.1364/JOSA.54.001060

[2] L. Fan and L. Lu. Design of a simple fisheye lens. Appl. Opt. 2019, 58(19), 5311-5319. https://doi.org/10.1364/AO.58.005311

[3] I. Powell. Panoramic lens. Appl. Opt. 1994, 33(31), 7356-7361. https://doi.org/10.1364/AO.33.007356

[4] G. Kweon, K. T. Kim, G. Kim, and H. Kim. Folded catadioptric panoramic lens with an equidistance projection scheme. Appl. Opt. 2005, 44(14), 2759–2767. https://doi.org/10.1364/AO.44.002759

[5] J. H. Wang, Y. C. Liang, and M. Xu. Design of panoramic lens based on ogive and aspheric surface. Opt. Express 2015, 23(15), 19489-19499. https://doi.org/10.1364/OE.23.019489

[6] W. Song, X. Liu, P. Lu, Y. Huang, D. Weng, Y. Zheng, Y. Liu, and Y. Wang. Design and assessment of a 360 °panoramic and high-performance capture system with two tiled catadioptric imaging channels. Appl. Opt. 2018, 57(13), 3429-3437. https://doi.org/10.1364/AO.57.003429

[7] C. Pernechele. Hyper Hemispheric Lens. Opt. Express 2016, 24(5), 5014-5019. https://doi.org/10.1364/OE.24.005014

[8] X. H. Wang, X. Zhong, R. F. Zhu, F. Gao, and Z. Q. Li. Extremely wide-angle lens with transmissive and catadioptric integration. Appl. Opt. 2019, 58(16), 4381-4389. https://doi.org/10.1364/AO.58.004381

[9] D. J. Brady and N. Hagen. Multiscale lens design. Opt. Express 2009, 17(13), 10659-10674. https://doi.org/10.1364/OE.17.010659

[10] D. J. Brady, M. E. Gehm, R. A. Stack, D. L. Marks, D. S. Kittle, D. R. Golish, E. M. Vera, and S. D. Feller. Multiscale gigapixel photography. Nature. 2012, 486(7403), 386-389. https://doi.org/10.1038/nature11150

[11] E. J. Tremblay, D. L. Marks, D. J. Brady, and J. E. Ford. Design and scaling of monocentric multiscale imagers. Appl. Opt. 2012, 51(20), 4691-4702. https://doi.org/10.1364/AO.51.004691

[12] P. Llull, L. Bange, Z. Phillips, K. Davis, D. L. Marks, and D. J. Brady. Characterization of the AWARE 40 wide-field-of-view visible imager. Optica. 2015, 2(12), 1086-1089. http://dx.doi.org/10.1364/OPTICA.2.001086

[13] W. Pang and D. J. Brady. Galilean monocentric multiscale optical systems. Opt. Express 2017, 25(17), 20332-20339. https://doi.org/10.1364/OE.25.020332

[14] D. Brady, W. Pang, H. Li, Z. Ma, Y. Tao, and X. Cao. Parallel cameras. Optica. 2018, 5(2), 127-137. https://doi.org/10.1364/OPTICA.5.000127

[15] G. M. Schuster, D. G. Dansereau, G. Wetzstein, and J. E. Ford. Panoramic single-aperture multi-sensor light field camera. Opt. Express 2019, 27(26), 37257-37273. https://doi.org/10.1364/OE.27.037257

[16] J. Duparré, P. Dannberg, P. Schreiber, A. Bräuer, and A. Tünnermann. Artificial apposition compound eye fabricated by micro-optics technology. Appl. Opt. 2004, 43(22), 4303-4310. https://doi.org/10.1364/AO.43.004303

[17] K. H. Jeong, J. Kim, and L. P. Lee. Biologically inspired artificial compound eyes. Science, 2006, 312(5773), 557-561. https://doi.org/ 10.1126/science.1123053

[18] L. Li and A. Y. Yi. Development of a 3D artificial compound eye. Opt. Express 2010, 18(17), 18125-18137. https://doi.org/10.1364/OE.18.018125

[19] Y. Song, Y. Xie, V. Malyarchuk, J. Xiao, I. Jung, K. Choi, Z. Liu, H. Park, C. Lu, R. Kim, R. Li, K. B. Crozier, Y. Huang, and J. A. Rogers. Digital cameras with designs inspired by the arthropod eye. Nature. 2013, 497(7447), 95-99. https://doi.org/10.1038/nature12083

[20] W. Lee, H. Jang, S. Park, Y. M. Song, and H. Lee. COMPU-EYE: a high resolution computational compound eye. Opt. Express 2016, 24(3), 2013-2026. https://doi.org/10.1364/OE.24.002013

[21] W. L. Liang, J. G. Pan, and G. D. J. Su. One-lens camera using a biologically based artificial compound eye with multiple focal lengths. Optica. 2019, 6(3), 326-334. https://doi.org/10.1364/OPTICA.6.000326

[22] I. Stamenov, A. Arianpour, S. J. Olivas, I. P. Agurok, A. R. Johnson, R. A. Stack, R. L. Morrison, and J. E. Ford. Panoramic monocentric imaging using fiber-coupled focal planes. Opt. Express 2014, 22(26), 31708-31721. https://doi.org/10.1364/OE.22.031708

[23] A. Arianpour, N. Motamedi, I. P. Agurok, and J. E. Ford. Enhanced signal coupling in wide-field fiber-coupled imagers. Opt. Express 2015, 23(4), 5285-5299. https://doi.org/10.1364/OE.23.005285

[24] S. J. Olivas, A. Arianpour, I. Stamenov, R. Morrison, R. A. Stack, A. R. Johnson, I. P. Agurok, and J. E. Ford. Image processing for cameras with fiber bundle image relay. Appl. Opt. 2015, 54(5), 1124-1137. https://doi.org/10.1364/AO.54.001124

[25] N. Motamedi, S. Karbasi, J. E. Ford, and V. Lomakin. Analysis and characterization of high-resolution and high-aspect-ratio imaging fiber bundles. Appl. Opt. 2015, 54(32), 9422-9431. https://doi.org/10.1364/AO.54.009422

[26] N. Motamedi, V. Lomakin, and J. E. Ford. Image restoration in fiber-coupled imagers using space-variant impulse response characterization. Appl. Opt. 2017, 56(14), 4003-4011. https://doi.org/10.1364/AO.56.004003

[27] W. M. Porter and H. T. Enmark. A System Overview of the Airborne Visible/Infrared Imaging Spectrometer (Aviris). Proc. SPIE 1987, 834, 22-31. https://doi.org/10.1117/12.942280

[28] R. W. Basedow, D. C. Carmer, and M. E. Anderson. HYDICE system: implementation and performance. Proc. SPIE 1995, 2480, 258-267. https://doi.org/10.1117/12.210881

[29] Y. Shen, Q. Yang*, B. Li. Ultrawide-field-of-view ultrahigh-spectral-resolution imaging spectrometer based on a grating-beamsplitter interferometer. Opt. Commun. 2025, 579, 131543. https://doi.org/10.1016/j.optcom.2025.131543

[30] Q. Yang. Design study of a compact ultra-wide-angle high-spatial-resolution high-spectral-resolution snapshot imaging spectrometer. Opt. Express 2021, 29(2), 2893-2908. https://doi.org/10.1364/OE.415484

[31] D. Mengu, A. Tabassum, M. Jarrahi, and A. Ozcan. Snapshot multispectral imaging using a diffractive optical network. Light Sci. Appl. 2023, 12(5), 789-808. https://doi.org/10.1038/s41377-023-01135-0

[32] W. Zhang, J. Suo, K. Dong, L. Li, X. Yuan, C. Pei, and Q. Dai. Handheld snapshot multi-spectral camera at tens-of-megapixel resolution. Nat. Commun. 2023, 14, 5043. https://doi.org/10.1038/s41467-023-40739-3

[33] Q. Yang. Static broadband snapshot imaging spectrometer. Opt. Eng. 2013, 52, 053003. https://doi.org/10.1117/1.OE.52.5.053003

[34] Q. Yang. Compact static infrared broadband snapshot imaging spectrometer. Chin. Opt. Lett. 2013, 12, 031201. https://doi.org/10.3788/COL201412.031201

[35] Q. Yang. Broadband high-resolution line-imaging spectrometer with a large working distance range. Opt. Commun. 2025, 583, 131802. https://doi.org/10.1016/j.optcom.2025.131802

[36] Y. Chen, J. Liang, B. Zhao, W. Yue, K. Zheng, Y. Zhao, Y. Qin, H. Nie, W. Wang, and J. Lv. Snapshot infrared Fourier transform imaging spectrometer for transient dynamic sensing. Opt. Express 2025, 33(3), 4024-4043. https://doi.org/10.1364/OE.550328

[37] J. Zhu, H. Nie, L. Wang, B. Zhao, K. Zheng, Y. Zhao, Y. Chen, W. Ning, P. Sun, X. Du, S. Ma, Y. Qin, W. Wang, J. Liang, and J. Lv. Snapshot hyperspectral imaging with high spatial resolution based on transformers. Opt. Express 2025, 33(15), 31731-31755. https://doi.org/10.1364/OE.56361